

1 **Development and application of a street-level meteorology and** 2 **pollutant tracking system (S-TRACK)**

3 Huan Zhang¹, Sunling Gong^{1*}, Lei Zhang^{1*}, Jingwei Ni², Jianjun He¹, Yaqiang Wang¹,
4 Xu Wang³, Lixin Shi⁴, Jingyue Mo¹, Huabing Ke¹, Shuhua Lu¹

5 ¹ State Key Laboratory of Severe Weather & Key Laboratory of Atmospheric Chemistry of CMA, Chinese Academy of
6 Meteorological Sciences, Beijing 100081, China

7 ² Henan Tianlang Ecological Technology Co. Ltd., Zhengzhou 450000, China

8 ³ Hangzhou Yizhang Technology Co., Ltd., Hangzhou 310000, China

9 ⁴ Key Laboratory of Meteorology and Ecological Environment of Hebei Province, Shijiazhuang 050000, China

10 *Correspondence to:* Sunling Gong (gongsl@cma.gov.cn) and Lei Zhang (leiz09@cma.gov.cn)

11 **Abstract.** A multi-model simulation system for street level circulation and pollutant
12 tracking (S-TRACK) has been developed by integrating the Weather Research and
13 Forecasting (WRF), the STAR-CCM+ (Computational Fluid Dynamics model - CFD) and
14 the Flexible Particle (FLEXPART) models. The winter wind environmental characteristics
15 and the potential contribution of traffic sources on nearby receptor sites in a city district of
16 China are analysed with the system for January 2019. It is found that complex building
17 layouts change the structure of the wind field and thus have an impact on the transport of
18 pollutants. The wind speed inside the building block is smaller than the background wind
19 speed due to the dragging effect of dense buildings. Ventilation is better when the
20 dominant airflow is in the same direction as the building layout. Influenced by the building
21 layout, the local circulations show that the windward side of the building is mostly the
22 divergence zone and the leeward side is mostly the convergence zone, which is more
23 obvious for high buildings. With the hypothesis that the traffic sources are uniformly
24 distributed on each road and with identical traffic intensity, the potential contribution ratios
25 (PCR) of four traffic sources to certain specific sites under the influence of the street-level
26 circulations are estimated with the method of residence time analysis. It is found that the
27 contribution ratio varies with the height of the receptor site. As a result of the generally

1 upward motion in the airflow, the position with the greatest PCR from the four road traffic
2 sources is located on a certain height which is commonly influenced by the distance of this
3 location from the traffic source and the background wind field (about 15m in this study).
4 The potential contribution of a road to one of the receptor sites is also investigated under
5 different wind directions. The established system and the results can be used to understand
6 the characteristics of urban wind environment and to help the air pollution control planning
7 in urban areas.

8 **1. Introduction**

9 In recent decades, with the continuous development of urban construction in China,
10 urban environmental problems have become increasingly serious and attracted widespread
11 attentions. According to the 2019 China Ecological Environment Status Bulletin, 180 of
12 337 cities at the prefecture level exceeded ambient air quality standards. The complex
13 building layouts and differences in thermal structures within cities lead to extremely
14 complicated meteorological characteristics and pollutant transport in urban areas (Lei et
15 al., 2012;Fernando et al., 2010;Aynsley, 1989). Though the transport of atmospheric
16 pollution in urban areas is widely studied, the study on tracking the sources of pollutants
17 on the street-level is still lacking due to limitations in research methods.

18 Researches on the street-level atmospheric environment are mainly divided into three
19 methods: field measurements (Macdonald et al., 1997), laboratory simulation research
20 (Mavroidis et al., 2003), and model simulations (Steenburgh et al., 2015;Hendricks et al.,
21 2007;Yucong et al., 2014). The model simulation has become one of the main methods for
22 studying environmental problems at the street-level due to the easy control of simulation

1 conditions and simple processing steps. The Computational Fluid Dynamics (CFD) is a
2 numerical simulation method to study the fluid thermal-dynamic problems and is now
3 widely used in the studies related to microscale problems within the urban canopy
4 (Gosman, 1999). The core of CFD simulation method is to solve the Navier-Stokes
5 equations. Depending on the turbulence closure scheme, CFD models can be divided into
6 three types: Direct numerical simulation (DNS), Reynolds-averaged Navier–Stokes
7 (RANS) (Liu et al., 2018;Zheng et al., 2015;Milliez and Carissimo, 2008)) and Large eddy
8 simulation (LES) (Kurppa et al., 2018;Li et al., 2008;Sada and Sato, 2002). The choice
9 among the three methods depends on the costs and objectives. One of the most important
10 issues using CFD simulation in the environment problems on the street-level is to obtain
11 accurate initial and boundary conditions (Ehrhard et al., 2000). To solve this problem, the
12 multi-scale coupling method is revealed as a good solution, which uses the meteorological
13 information from mesoscale model as the initial and boundary conditions to drive CFD
14 (Nelson et al., 2016). Tewari et al. (2010) proved that the CFD simulation was improved
15 significantly when the results of Weather Research and Forecasting (WRF) model were
16 used as the initial and boundary conditions. With the WRF model, the community
17 multiscale air quality (CMAQ) model, and the CFD (RANS) approach, Kwak et al. (2015)
18 built an urban air quality modelling system, which presented a better performance than the
19 WRF-CMAQ model in simulating nitrogen dioxide (NO₂) and ozone (O₃) concentrations.

20 Nevertheless, the street-level air pollutant transport resulted from the nearby sources
21 was still not fully investigated. The Flexible Particle (FLEXPART) model (Stohl et al.,
22 2005;Stohl, 2003) is a gas-block trajectory-particle dispersion model based on the
23 Lagrangian particle method. The FLEXPART model can track the transport of tracers via

1 forward or backward simulation. Different from Eulerian model, the Lagrangian model is
2 not restricted by the Courant–Friedrichs–Lewy (CFL) condition (Stam, 1999) and thus, the
3 integration process in the Lagrangian model can be maintained with high spatial resolution
4 with acceptable computation efficiency. Initially, the FLEXPART model was driven by
5 global meteorological reanalysis data from European Centre for Medium-Range Weather
6 Forecasts (ECMWF) or National Centers for Environmental Prediction (NCEP). Fast and
7 Easter (2006) developed a FLEXPART version that used the WRF model output and was
8 optimized with technical level and output results. Nowadays, the WRF-FLEXPART model
9 has been widely used to research the regional transport of air pollutants (Yu et al., 2020;He
10 et al., 2020;Gao et al., 2020;He et al., 2017a;Brioude et al., 2013;de Foy et al., 2011). Cécé
11 et al. (2016) firstly applied the FLEXPART model at a small-scale resolution to analyse
12 potential sources of nitrogen oxide (NO_x) in urban areas, with the WRF model results as
13 the driving field. Though FLEXPART has been extensively applied in medium and long-
14 range transport cases (Madala et al., 2015;Heo et al., 2015;Sandeepan et al., 2013;Liu et
15 al., 2013), it has been rarely tested for street-level transport and small-scale resolution grids.

16 The objective of the present work is to investigate the flow field characteristics and
17 potential contribution of traffic sources to receptor sites, under real building scenarios and
18 meteorological conditions. To this end, a multi-model simulation system for street level
19 circulation and pollutant tracking (S-TRACK) was developed by integrating the WRF
20 mesoscale, the STAR-CCM+ street scale and the FLEXPART particle dispersion models,
21 and applied to the Jinshui District of Zhengzhou city, Henan Province. Zhengzhou is
22 located in the central of China with four distinct seasons. According to the Oceanic Niño
23 Index (ONI), an El Niño event occurred in January 2019. The occurrence of El Niño

1 generally favours a warm winter and weak winter winds in China that is conducive to
2 occurrence of air pollution. Therefore, the period of January 2019 was selected and
3 simulated for this study. This manuscript is organized as follows. Section 2 presents the
4 model details and the observed data for the model validation. Section 3 provides the details
5 of the model validation results, the wind environment characteristics and the potential
6 contribution of traffic source on receptor sites in the region. Section 4 provides the
7 conclusions of the study.

8 **2. Data and Methods**

9 **2.1 S-TRACK description**

10 The S-TRACK system consists of three major components (Fig. 1). The WRF model
11 is used to obtain the mesoscale three dimensions (3D) meteorological fields, with the initial
12 and boundary conditions provided by NCEP FNL reanalysis data. The STAR-CCM+,
13 driven by the meteorological data from WRF, is used to compute the refined 3D street-
14 level meteorological fields with a resolution of 1 m to 100 m in the simulation area. With
15 the refined 3D meteorology, the FLEXPART model is run to analyse the transports of
16 traffic sources at street-level and their potential contribution to specific sites. One should
17 note that some meteorological variables needed by FLEXPART that the STAR-CCM+
18 cannot provide (Table 1) are obtained from WRF simulations. The specific coupling
19 scheme of the S-TRACK system is detailed as follows:

20 **I. Run the WRF model** (refer to Section 2.2 for specific settings) to obtain
21 meteorological data with a spatial resolution of $1 \text{ km} \times 1 \text{ km}$, including temperature,
22 pressure, humidity, wind, etc.

1 **II. Extract the value of temperature (T) and wind (U, V and W)** from the WRF
2 simulation, as the initial and boundary conditions of the STAR-CCM+ simulation. Run the
3 STAR-CCM+ (refer to Section 2.3 for specific settings) to obtain values of meteorological
4 variables with a spatial resolution of 1 m - 100 m, including wind field, surface pressure,
5 and surface sensible heat flux, etc. The 3D street-level grid for STAR-CCM+ is detailed
6 in Section 2.3.1.

7 **III. Match the STAR-CCM+ grids to the WRF grids.** As the FLEXPART-WRF
8 (version 3.3.2) was used here, the grid structure of meteorological input data to
9 FLEXPART should match the grid structure of WRF model. To this end, a regular fine
10 grid with a horizontal resolution of 10×10 m was constructed based on the pre-processing
11 system of WRF model (WPS). The urban building height data obtained based on drone
12 aerial photography was taken as part of the terrain height data in the WPS. Once the refined
13 grid was established, the meteorological variables of the STAR-CCM+ and WRF model
14 were interpolated into the grid by a nearest-neighbour interpolation method.

15 **IV. Run the backward FLEXPART model** (refer to Section 2.4 for specific settings)
16 to obtain the 3D spatial location data of released particles, which was used to analyse the
17 features of pollutant transport at street-level and potential contribution of traffic source to
18 specific sites.

19 **2.2 WRF model configuration**

20 In this study, the WRF model is configured with four nested domains (Fig. 2a), with
21 the resolution of 27 km × 27 km (85 × 85 grid cells), 9 km × 9 km (82 × 82 grid cells), 3
22 km × 3 km (82 × 82 grid cells), and 1 km × 1 km (61 × 61 grid cells), respectively.

1 Vertically, there are 45 full eta levels from the surface to 100 hPa with 11 levels below 2
2 km, on which the meteorological fields are used to drive the STAR-CCM+. The innermost
3 nested region is shown in Fig. 2b, where the area focused in this study is marked with a
4 black box. The initial and boundary conditions of WRF model are obtained from the NCEP
5 re-analysis data (<http://rda.ucar.edu/dataset-s/ds083.2>). The boundary conditions are
6 updated every 6 hr. Table 2 lists the selected physical parameterization schemes. The time
7 from 12:00 Beijing time (BJT) on December 30, 2018 to 23:00 BJT on January 31, 2019
8 is chosen as the modelling period, with the simulation results recorded every hour.

9 **2.3 STAR-CCM+ configuration**

10 The STAR-CCM+, one of the most commonly used commercial CFD software, was
11 selected for the street-level simulation. Previous studies had found an excellent correlation
12 between STAR-CCM+ simulated and measured values in simulating environmental and
13 meteorological problems at street-level (Santiago et al., 2017;Borge et al., 2018;Jls et al.,
14 2020). The model has functions such as geometric modelling, model pre-processing, the
15 calculation execution, and post-processing of results. More details on STAR-CCM+ can
16 be found at
17 [https://www.plm.automation.siemens.com/global/zh/products/simcenter/STAR-](https://www.plm.automation.siemens.com/global/zh/products/simcenter/STAR-CCM.html)
18 [CCM.html](https://www.plm.automation.siemens.com/global/zh/products/simcenter/STAR-CCM.html).

19 **2.3.1 3D street-level grid generation**

20 The establishment of a 3D geometric model is based on the actual terrain and
21 buildings height data for the simulated area obtained through the drone aerial photography
22 technology. The basic data such as the geometric shape of urban buildings, roof height and

1 vector data of the top of buildings with high resolution, high timeliness and accuracy are
2 used to construct a realistic 3D geometric model for driving the STAR-CCM+ simulation.
3 In the process of model construction, the same shape as the actual building was maintained
4 to reduce the influence of model errors on the calculation results (Fig. 3a). The length,
5 width, and height of the STAR-CCM+ calculation domain are 13 km, 11 km, and 2 km,
6 respectively, among which, nearly 2/3 of the buildings are distributed in the range of 10 -
7 40 meters, with the average height of the buildings of 32 m. The highest building in the
8 area is 390 m, and the lowest building is 6 m.

9 The geometric model domain is divided by polyhedral meshes (Fig. 3c). The
10 polyhedral mesh has much fewer cells than the traditional tetrahedral mesh, but with a
11 similar accuracy of calculation. Under the same number of grid cells, the numerical
12 simulation results of polyhedral grid cells are more consistent with experimental data than
13 tetrahedral grid cells (Zhang et al., 2020). The grid cells on the ground and near the
14 buildings are much denser (Fig. 3b) (the minimum resolution is about 1 m), so that the
15 influence of the building on the flow patterns can be described more accurately. In the end,
16 the number of unit grid cells generated is 382181, and the number of nodes is 1990224.

17 **2.3.2 Physical model and boundary conditions**

18 The STAR-CCM+ solves the RANS with the realizable $k-\varepsilon$ turbulence closure
19 scheme in this study (Li et al., 2019; Li et al., 2006; Lei et al., 2004). The ground and
20 building surfaces are set to be no-slip, and the distribution of fluid velocity and pressure
21 near the ground and the building surface is described by the blended wall function. For the
22 coupling of WRF model to STAR-CCM+, the values of temperature and wind from the

1 WRF simulation are extracted to establish the initial and boundary conditions for STAR-
2 CCM+. Since the variables obtained by WRF simulation have a relatively coarse resolution
3 of 1 km, the velocity components (U, V and W) and the temperature are interpolated to the
4 boundary of STAR-CCM+ domain using the spline interpolation method and the linear
5 interpolation method, respectively. For the turbulence intensity and turbulence viscosity
6 ratio, the lateral and upper boundaries are set as constants with values of 0.1 and 10,
7 respectively.

8 **2.4 FLEXPART configuration**

9 The simulation area is set to sub-domain B in Figure 3, with a horizontal grid
10 resolution of $10\text{ m} \times 10\text{ m}$. The simulation time is from 1:00 BJT 1 January 2019 to 23:00
11 BJT 30 January 2019. The time step of FLEXPART is 1 s, and the output time interval is
12 120 s. Through backward trajectory simulation, the impact of traffic source on the receptor
13 sites in the region can be effectively analysed. Due to the high number of grid cells in the
14 region and the fact that increasing the number of released particles leads to consuming
15 more computational resources, the particle residence time is set as 2 h, and 5 tracer
16 particles are released per hour, and the total number of particles released was 3590.

17 **2.5 Meteorological observation data**

18 Hourly near-surface meteorological observations from the Bank School City
19 monitoring site (hereinafter referred as the BSC monitoring site), including 2 m
20 temperature (T), 2 m relative humidity (RH), surface pressure (P), 10 m wind direction
21 (WD) and 10 m wind speed (WS) in January 2019 are used to evaluate the WRF and
22 STAR-CCM+ simulation results, with the statistical indexes including Pearson's

1 correlation coefficient (R), root mean square error (RMSE), mean bias (MB) and mean
2 error (ME). The location of the BSC monitoring site (34.802375N, 113.675237E) is shown
3 in Figure 3.

4 **3. Results and discussions**

5 **3.1 Model evaluation**

6 The performance of WRF model to simulate meteorological elements is an important
7 basis for STAR-CCM+ and FLEXPART simulations. The hourly meteorological data for
8 January 2019 obtained from the innermost nested simulation of the WRF model is selected
9 to compare with observation data to verify the WRF model. Table 3 lists the statistical
10 results of T, RH, P, and WS. The T and RH are slightly underestimated, with the MB
11 values as -1.86 k and -5.95%, respectively, and the P and WS are overestimated by the
12 WRF model, with the MB values as 3.66 hPa and 1.44 m s⁻¹, respectively. The R values
13 for T, RH and P are 0.80, 0.70 and 0.98, respectively, passing the 99% significance test
14 (see Appendix 2), and indicating that the variation characteristics of T, RH and P are well
15 reproduced by the WRF model. WS is generally overestimated by WRF model (Temimi
16 et al., 2020;He et al., 2014), which is also found in the present study with the RMSE of
17 1.97 m s⁻¹. The performance of the near-surface meteorology obtained by the WRF
18 simulation is equivalent to previous studies (He et al., 2017b;Carvalho et al., 2012).

19 Since the time-varying boundary conditions in the calculation domain of STAR-
20 CCM+ are obtained from WRF model, the simulation performance of WRF model has an
21 important influence on the STAR-CCM+ simulation results. The wind has an important
22 influence on the transport of air pollutants in the area (Zhang et al., 2015). Figure 4 shows

1 the hourly wind observations and simulations at the BSC monitoring site in January 2019.
2 Both WRF and STAR-CCM+ overestimate the wind speed to certain degrees (Fig. 4a).
3 The average of observed wind speed is 0.92 m s^{-1} , and the average of simulated value by
4 WRF and STAR-CCM+ is 2.37 m s^{-1} and 2.00 m s^{-1} , respectively. The R values of WRF
5 and STAR-CCM+ are 0.45 and 0.67, respectively, passing the 99% significance test, and
6 demonstrating the refined STAR-CCM+ wind simulations are superior to that of the WRF.
7 This might be due to the fact that the resolution of WRF simulation is not fine enough and
8 the underlying surface is processed in a parameterized way that can't accurately describe
9 the urban surface roughness. For the STAR-CCM+, the geometric model is used for the
10 underlying surface, which could better reflect the urban surface conditions compared to
11 parametric methods. Figure 4b shows the comparison results of the observed and simulated
12 wind directions. It can be seen that the change of the wind direction is captured by the
13 STAR-CCM+ well. The wind direction is verified by hit rates (HR) (Schlünzen and Sokhi,
14 2008) , which is a reliable overall measure for describing model performance (see
15 Appendix 4). With desired accuracy between $\pm 45^\circ$, the HR are calculated at 63 and 51 %
16 for STAR-CCM+ and WRF, respectively, indicating that variations in wind direction have
17 been basically captured with a better performance for STAR-CCM+ simulations.

18 **3.2 The characteristics of the street-level wind fields**

19 In urban areas, the complex spatial structure and layout of buildings have a great
20 influence on the street-level wind field (Liu et al., 2018; Park et al., 2015), which is a crucial
21 meteorological factor that controls the transport of air pollutants. The street-level wind
22 field characteristics were simulated by the S-TRACK and discussed comprehensively in

1 this paper for the overall average in January as well as for different background wind
2 directions, i.e., north, south, west and east, respectively.

3 **3.2.1 The average wind field characteristics**

4 Figures 5a-b illustrate the distribution of the average wind streamlines in January at
5 the height of 5 m and 40 m, respectively. At the height of 5 m, the wind field structure is
6 more complicated (Fig. 5a) than that at 40 m (Fig. 5b). The wind speed is relatively more
7 intense in the areas where the buildings are sparse and smaller. In addition, the flow fields
8 diverge or converge due to the layout of buildings and streets, causing the wind direction
9 inside blocks differ from the background wind direction greatly. As the density of
10 buildings gradually decreases with the increases of height, this phenomenon diminishes,
11 reflected by the relatively more consistent wind fields at 40 m (Fig. 5b). The phenomenon
12 was also found in a previous study (Sui et al., 2016).

13 To clearly show the details of the wind field, a sub-domain A (Fig. 3a) with complex
14 building structures is selected from the entire computational domain. The near-surface
15 winds disperse or converge horizontally and rise or subsidence vertically with the building
16 (Fig. 5c). During the climb or fall with the building, downwash winds with high wind
17 speeds occur (as shown in the red dashed circles). Due to the complexity of the building
18 layout, local circulation is formed on the west side of the BSC monitoring site, making the
19 airflow around the building on the south side of the station accumulate and forms an
20 obvious convergence area (Fig. 5c), which is not conducive to the air circulation and
21 pollution transport (as shown in the red box).

1 3.2.2 The wind field characteristics under different background wind directions

2 Figure 6 shows the distributions of near-surface wind and its divergence under four
3 different background wind directions. In general, the overall wind direction in the area is
4 consistent with the background wind direction, but the airflow near-surface is significantly
5 affected by the building layout, thus forming local circulations with divergence or
6 convergence zones. The wind speeds in the areas with dense buildings are significantly
7 smaller than those in open areas (Figs. 6a-1, 6b-1, 6c-1, and 6d-1), which is attributed to
8 the obvious frictional dragging effect of the dense buildings. The overall wind direction in
9 the area is generally the same as the background wind direction, but the airflow is diverged
10 or converged by the influence of the building layout, resulting in a great difference in wind
11 direction inside the block from the background. When the background wind direction is
12 north or west (Figs. 6b and 6c), the overall wind speed in the area is relatively large. This
13 is mainly due to the temperate monsoon climate in Zhengzhou, where northwest and west
14 winds prevail in winter and wind speeds are relatively high.

15 It is found that the windward side of the building is mostly a divergence zone and the
16 leeward side is mainly a convergence zone, which is more obvious for higher buildings.
17 When the airflow meets the building, the airflow on the windward side of the building is
18 blocked and thus spreads outward, forming a divergence zone; while the airflow on the
19 leeward side of the building converges and generates a vortex with lower wind speed,
20 forming a convergence zone. For example, at BSC monitoring site, when the background
21 wind direction is west, the wind speed on the windward side of the building is higher and
22 diffused outward by the building blockage (Fig. 6c-2), resulting in a significant divergence
23 zone (Fig. 6c-3). High-rise buildings have a greater impact on the wind field and cause a

1 strong degree of convergence and divergence. It can be seen that the degree of divergence
2 or convergence around the high-rise building is more significant than those around low
3 buildings in the area (Figs. 6b-3, 6c-3, and 6d-3). In addition, the ventilation is better when
4 the dominant airflow is in the same direction as building layout (Fig. 6c). In the process of
5 urban construction, the influence of prevailing wind direction on the layout of buildings
6 should be considered, which could effectively improve the efficiency of urban ventilation.

7 **3.3 Potential contribution of traffic sources**

8 In this section, the S-TRACK system is used to analyse potential contribution of main
9 traffic roads (R1-R4) in sub-domain B (Fig. 3a) on several receptor sites nearby with
10 different heights and locations with a number of schools and residential areas. The widths
11 of roads R1-R4 are about 45, 33, 20 and 18 meters, respectively. Since the detailed
12 information on road traffic emissions was not available, the road traffic emissions were
13 assumed to be uniformly distributed and with identical intensity in this study. During the
14 backward trajectory simulation, the particles as long as passing within 5 m height above
15 the road is considered to be a potential contribution from the road emissions to the receptor
16 site. Additionally, the potential contribution of traffic source under different background
17 wind directions was also explored. The residence-time analysis (RTA), which has been
18 previously used to identify the accounted contribution of emission sources to air quality of
19 receptors (Yu, 2017; Salvador et al., 2008; Hopke et al., 2005; Poirot et al., 2001; Ashbaugh
20 et al., 1985), was selected in this study to assess the potential contribution ratio (PCR) of
21 the traffic source on receptors. The RTA is expressed as:

$$22 \quad R_{i,j} = \frac{\tau_{i,j}}{t},$$

1 where $R_{i,j}$ indicates the contribution ratio of the grid (i,j) to receptor; $\tau_{i,j}$ means the
2 residence time in the grid (i,j) and t means the total residence time in all grid cells.

3 **3.3.1 Potential contribution of traffic source at different sites in winter**

4 In order to analyse the potential contribution of the traffic source on different
5 locations, the receptor sites were selected at different locations and heights, and the overall
6 PCR of all wind directions for January 2019 was calculated by RTA (Table 4). Receptor
7 sites S2-S8, with identical horizontal location but different heights, are selected to
8 investigate contributions of traffic source to receptor sites at different heights. The PCR of
9 all the four roads are 4.05%, 4.25%, 4.33%, and 4.67% for receptor sites S2 to S5, with
10 the height of 2 m, 5 m, 10 m, and 15 m, respectively. However, as the receptor height
11 continues to rise, namely from S5 to S8, the PCR of the roads gradually decrease from
12 4.67% to 3.55% (Table 4). It's noteworthy that the contributions from R1 and R3 are
13 primary, especially the R1, which may be due to the closer distance to the site and the
14 generally northeast wind field. The potential contribution of the traffic source is the
15 greatest when the receptor site is located at a height of 15 m, suggesting the air quality at
16 that height is most susceptible to traffic emissions under the northeast wind field. In
17 addition, according to density distribution (refers to the number of particles that have
18 stayed in the space of 10 m × 10 m in the horizontal direction and 5 m from the surface to
19 above in the vertical direction) of all trajectory points that have passed through the traffic
20 roads (Figs. 7), it can be seen that the road section with large potential contribution to the
21 receptor sites generally located to their northeast, which might be a result of the
22 combination effect of the background wind field and the building layout. For more details,

1 the vertical structure of winds along the direction of the wind field at the receptor site S2
2 (Fig. 8b) is also presented. It can be seen that there is a general upward motion in the
3 airflow, making the position with the greatest PCR from traffic source locate at a certain
4 height, which is about 15 m over the receptor site S2 in this case.

5 It can be seen from Table 4 that R1 is the road with the greatest potential contribution
6 to the receptor sites. The horizontal distance between road R1 and the receptor sites is
7 about 300 m and the peak of the PCR occurs at a height of about 15 m (corresponding to
8 the site S5). However, for the road R3, which is closest to the receptor sites in horizontal
9 (about 200 m), the contribution ratios are lower than those of the road R1. Figure 8a shows
10 that the near ground winds are generally northeast, resulting in that the probability of traffic
11 contributions from R1 and R3 road sections upwind of the site S2 is roughly the same.
12 Nonetheless, as mentioned in section 3.3, the width for the road R1 is about twice of that
13 for the road R3. Therefore, even R1 was a little farther from the receptor sites than R3, the
14 contribution ratios of R1 to the sites were calculated larger than those of R3. For the R2
15 and R4, the distance from the receptor sites is about 1200 and 1500 m, respectively, far
16 away than those of R1 and R3. In addition, under the northeast winds, traffic source was
17 hardly transported to the receptor sites, rendering the contribution ratios quite small below
18 50 m (Table 4). It can also be seen, from Table 4, that the corresponding PCR of R2 and
19 R4 may peak at a height over 50 m.

20 Since the road R1 had the largest potential contribution to the receptor sites, the
21 contribution of R1 to different positions is focused in the subsequent discussion. For the
22 receptor site S1, which is about 400 m from the R1, located in a dense building area with
23 the building height at 30 to 40 meters, the PCR of the traffic source on the receptor site is

1 calculated to be 1.81%. For the receptor site S2, which is about 300 m from the traffic road,
2 located in an open area and surrounded by low buildings, the PCR of the traffic source is
3 determined to be 2.38%. It might be inferred that the wind field difference partially resulted
4 from the influence of buildings layout led to the higher contribution ratio to S2. From the
5 average wind field in January 2019 (Fig.8a), it can be seen that the winds were influenced
6 by high-rise buildings around the S1, resulting in a change in transport path of pollutants
7 and thus, making pollutants difficult to reach the S1 site. However, for S2 site, the winds
8 were less influenced by the buildings and pollutants were more easily transported there.

9 **3.3.2 Potential contribution of traffic source under different background wind** 10 **directions**

11 In order to investigate the potential contribution of traffic source under different
12 background wind directions, the receptor site S2 influenced by the R1 under the east, the
13 south, the west, and the north wind directions was classified from the simulation period.
14 The PCR of traffic source were estimated to be 2.45%, 0.07%, 1.98%, and 2.97% for the
15 east, the south, the west, and the north wind directions, respectively, revealing that the
16 difference in potential contribution was largest between the south and north wind
17 directions. When the background wind direction was south, the receptor site was located
18 upwind of the road, and the road traffic source contributed very little to the receptor site.
19 On the contrary, when the receptor site was downwind of the road with northern winds,
20 the contribution ratio of road traffic source to the receptor site was the greatest. When the
21 background wind direction was east and west, the contribution ratio to the receptor point
22 was similar, ranging between the ratios under south and north wind directions. The lower

1 contribution ratio during westerly winds relatively to that under easterly winds might
2 partially be due to the denser distribution of buildings upwind of the receptor site. Complex
3 building layouts changed the structure of the wind field and thus had an impact on the
4 transport of pollutants. The slow air circulation in dense building areas made it
5 unfavourable for pollutants to be transported. In the windward side of the dense building
6 area, the wind was blocked and diverted to both sides of the building. Pollutants were
7 difficult to transport to the leeward side of the building, where the receptor site was located.
8 The results of the potential contribution of traffic source under different background wind
9 conditions is helpful to understand the street-level pollution transport characteristics and
10 provides effective suggestions for the traffic pollution control strategies.

11 **4. Conclusions**

12 A street-level pollutant tracking system has been developed to simulate micro-scale
13 meteorology and used to analyse the characteristics of wind environment and the potential
14 traffic source contribution of air pollution to receptors through backward simulations in a
15 city district. In general, the S-TRACK system is effective in simulating the street-level
16 meteorological and pollution problems. The presence of buildings has a significant effect
17 on the wind environment, i.e., the dragging effect of dense buildings renders the wind
18 speed inside the block smaller than the background wind speed. The ventilation is better
19 when the dominant airflow is consistent with the direction of building layout. Influenced
20 by the building layout, the airflow near-surface is formed with divergence and convergence
21 zones. The windward side of the building is mostly a divergence zone and the leeward side
22 is mostly a convergence zone, which is more obvious for higher buildings.

1 As a test case, the S-TRACK system has been used to investigate the potential
2 contribution of traffic source on receptor sites with different locations, heights and
3 background wind directions in a city district. For a specific location of this case study, the
4 potential traffic contribution ratios also varied with height at about 4.05%, 4.25%, 4.33%,
5 4.67%, 4.38%, 3.64% and 3.55% for 2, 5, 10, 15, 20, 40, 50 m, respectively, manifesting
6 a significant trend of increasing and then decreasing with height. In addition, the height of
7 position with the greatest PCR from the traffic source varies jointly influenced by the
8 distance between the position and traffic source, as well as the background wind field. The
9 potential contribution of traffic sources on a specific receptor site varies under different
10 background wind directions, which are estimated to be 2.45%, 0.07%, 1.98%, and 2.97%
11 for the east, the south, the west, and the north wind directions, respectively. The difference
12 in potential contribution under east and west wind directions might partially be due to the
13 density of buildings upwind of the receptor site.

14 In the future, in-depth simulation experiments with different building layouts, wind
15 field environments, and distances between traffic source and receptor are required to
16 quantify the potential contribution of street-level pollution sources and to establish the
17 relationship between meteorological conditions, buildings and various emissions (point,
18 area and line sources) in the street-level for an effective management of regional pollution
19 in a city.

1 Appendix

2 1. Some settings to improve the calculations efficiency of CFD

3 It is true that using a CFD model for the atmospheric numerical simulation has the
4 problem of high computational cost. In this study, the RANS is chosen as the CFD model,
5 which requires relatively small amount of computational resources. The time step of
6 STAR-CCM+ is set to 60s, with a maximum of 20 internal iterations in each time step and
7 a parallel computing with 32 CPUs is done on a supercomputer. The simulation error
8 increases with the simulation time. In order to ensure the efficiency and accuracy of the
9 simulation, the month was divided into four time periods to simulate, as shown in Table
10 A1.

11 **Table A1. The division of each simulation time period and the physical time spent on the simulation**

Simulation start time	Simulation end time	Length of simulation time	Physical time spent
2018/12/31 00:00:00	2019/1/09 04:00:00	220h	126.45h
2019/1/08 00:00:00	2019/1/17 04:00:00	220h	128.33h
2019/1/16 00:00:00	2019/1/25 04:00:00	220h	128.53h
2019/1/24 00:00:00	2019/2/01 08:00:00	200h	117.10h

12

13 2. Significance test

14 Significance test is used to determine the significance of the results in relation to the
15 null hypothesis, with a p-value, or probability value describing how likely the data would
16 have occurred by random chance (i.e. that the null hypothesis is true). A p-value less than
17 0.05 (typically ≤ 0.05) is statistically significant. It indicates strong evidence against the
18 null hypothesis, as there is less than a 5% probability the null is correct.

1 **3. The observed data for January 2019 at various meteorological stations in**
2 **Zhengzhou city.**

3 **Table A2. The location of each meteorological station and the average wind speed.**

number	Latitude and longitude coordinates	Average wind speed
1	(34.7274 N, 113.7493 E)	0.92 m s ⁻¹
2	(34.73506 N, 113.6457 E)	0.92 m s ⁻¹
3	(34.7466 N, 113.6876 E)	1.32 m s ⁻¹
4	(34.76117 N, 113.6883 E)	0.61 m s ⁻¹
5	(34.78245 N, 113.6567 E)	1.51 m s ⁻¹
6	(34.81151 N, 113.6948 E)	1.48 m s ⁻¹
7	(34.83267 N, 113.5453 E)	0.72 m s ⁻¹

4
5 **4. Hit rates**

6 The hit rate is a reliable overall measure for describing model performance.

$$H = \frac{100}{m} \times \sum_{i=1}^m n_i$$

7 with $n_i = \begin{cases} 1 & \text{for } |\text{difference (measurement,} \\ & \text{model result)}| < A \\ 0 & \text{for } |\text{difference (measurement,} \\ & \text{model result)}| > A \end{cases}$

8 where m is the number of comparison data, A is to consider the desired model accuracy.

9 The single hit rate is calculated ranging from 100% if all model results are within A of the
10 observations to 0% if none are.

11 **5. Divergence**

12 The divergence is a quantity that describes the degree to which air converges from its
13 surroundings to a point or flows away from a point. It is used to describe the intensity of
14 divergence and convergence at locations in space. The formula is as follows.

15
$$\text{div } \mathbf{v} = \nabla \cdot \mathbf{v} = \frac{\partial u_i}{\partial x_i} = \frac{\partial u}{\partial x} + \frac{\partial v}{\partial y} + \frac{\partial w}{\partial z},$$

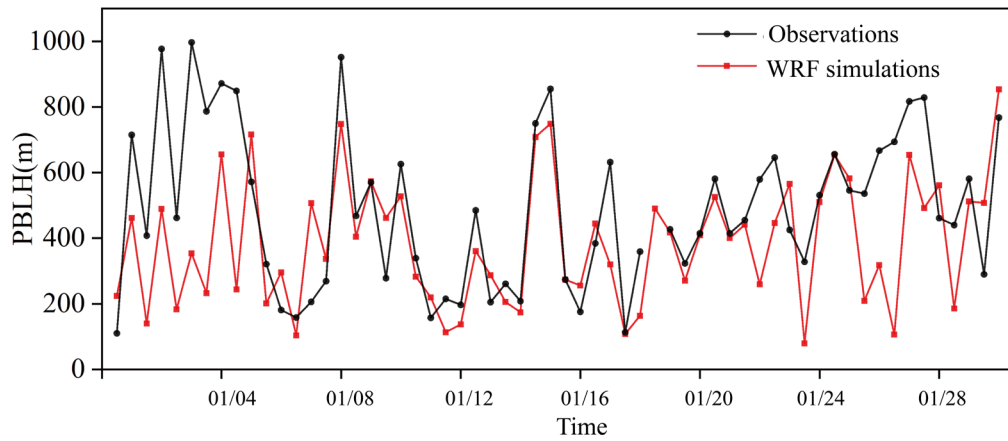
1 where u , v and w are the components of the wind in the x , y and z direction, respectively.
2 When the $div \mathbf{v} < 0$, the location is convergence; when the $div \mathbf{v} > 0$, the location is
3 divergence.

4 **6. PBLH validation**

5 The bulk Richardson number (Ri) method was taken to estimate the BLH base on the
6 sounding data of Zhengzhou. Ri is expressed as:

$$7 \quad R_i(z) = \frac{(g / \theta_{vs})(\theta_{vz} - \theta_{vs})(z - z_s)}{(u_z - u_s)^2 + (v_z - v_s)^2 + (bu_*^2)},$$

8 where z is the height above ground, s the surface, g means the acceleration of gravity, θ_v
9 the virtual potential temperature, u and v the component of wind speed, and u_* the surface
10 friction velocity. u_* can be ignored here due to it is small relative to the wind shear
11 (Vogelezang and Holtslag, 1996). Previous theoretical and laboratory studies suggested
12 that when Ri is smaller than a critical value (~ 0.25), the laminar flow becomes unstable
13 (Stull, 1988). Therefore, the lowest level z at which the interpolated Ri exceeds the critical
14 value of 0.25 is referred to as PBLH in this study, which is referred to the criterion used
15 by Seidel et al. (2012). The R value is 0.57, passed the 99% significance test. It can be
16 seen from Figure A1 that the variation of boundary layer height is generally captured.



1

2 **Figure A1. Time series of the observed (black) and simulated (red) PBLH at 8:00 and 20:00 Beijing**
 3 **time (BJT) in Zhengzhou sounding site.**

4

5 **Code/data availability**

6 All source code and data can be accessed by contacting the corresponding authors Sunling

7 Gong (gongsl@cma.gov.cn) and Lei Zhang (leiz09@cma.gov.cn).

8 **Authors contribution**

9 Sunling Gong and Lei Zhang designed the research. Huan Zhang performed the

10 simulations and wrote the manuscript with suggestions from all authors. Jingyue Mo,

11 Huabing Ke , Xu Wang and Shuhua Lu assisted with data processing. Jianjun He, Yaqiang

12 Wang, Jingwei Ni and Lixin Shi participated in the scientific interpretation and discussion.

13 All authors contributed to the discussion and improvement of the manuscript.

14 **Competing interests**

15 The authors declare that they have no conflict of interest.

1 **Acknowledgments**

2 The authors would like to acknowledge Bin Cui and Lin Zhang from Peking University
3 and Liangfu Chen from Chinese Academy of Sciences for their valuable suggestions to
4 improve the article.

5

1 References

- 2 Ashbaugh, L., Malm, W., and Sadeh, W.: A residence time probability analysis of sulfur concentrations at grand Canyon
3 national park, *Atmos. Environ.*, 19, 1263-1270, [https://doi.org/10.1016/0004-6981\(85\)90256-2](https://doi.org/10.1016/0004-6981(85)90256-2), 1985.
- 4 Aynsley, R.: Politics of pedestrian level urban wind control, *Build Environ*, 24, 291-295, [https://doi.org/10.1016/0360-1323\(89\)90022-X](https://doi.org/10.1016/0360-1323(89)90022-X), 1989.
- 6 Borge, R., Jose Luis Santiago, David de la Paz, Fernando Martín, Jessica Domingo, Cristina Valdés, Beatriz Sánchez, Esther
7 Rivas, Ma Teresa Rozas, Sonia Olaechea Lázaro, Pérez, J., and Fernández, a. Á. L.-P.: Application of a short term air quality
8 action plan in Madrid (Spain) under a high-pollution episode - Part II: Assessment from multi-scale modelling, *Sci. Total*
9 *Environ.*, 635, 1574-1584, <https://doi.org/10.1016/j.scitotenv.2018.04.323>, 2018.
- 10 Brioude, J., Arnold, D., Stohl, A., Cassiani, M., Morton, D., Seibert, P., Angevine, W., Evan, S., Dingwell, A., Fast, J. D.,
11 Easter, R. C., Pisso, I., Burkhardt, J., and Wotawa, G.: The Lagrangian particle dispersion model FLEXPART-WRF version
12 3.1, *Geosci. Model Dev. (GMD)*, 6, 1889-1904, <https://doi.org/10.5194/gmd-6-1889-2013>, 2013.
- 13 Carvalho, D., Rocha, A., Gómez-Gesteira, M., and Santos, C.: A sensitivity study of the WRF model in wind simulation for
14 an area of high wind energy, *Environ. Model. Software*, 33, 23-34, <https://doi.org/10.1016/j.envsoft.2012.01.019>, 2012.
- 15 Cécé, R., Bernard, D., Brioude, J., and Zahibo, N.: Microscale anthropogenic pollution modelling in a small tropical island
16 during weak trade winds: Lagrangian particle dispersion simulations using real nested LES meteorological fields, *Atmos.*
17 *Environ.*, 139, 98-112, <https://doi.org/10.1016/j.atmosenv.2016.05.028>, 2016.
- 18 Chen, F., and Dudhia, J.: Coupling an Advanced Land Surface-Hydrology Model with the Penn State-NCAR MM5 Modeling
19 System. Part I: Model Implementation and Sensitivity, *Mon. Weather Rev.*, 129, 569-585, [https://doi.org/10.1175/1520-0493\(2001\)129<0569:CAALSH>2.0.CO;2](https://doi.org/10.1175/1520-0493(2001)129<0569:CAALSH>2.0.CO;2), 2001.
- 21 de Foy, B., Burton, S. P., Ferrare, R. A., Hostetler, C. A., Hair, J. W., Wiedinmyer, C., and Molina, L. T.: Aerosol plume
22 transport and transformation in high spectral resolution lidar measurements and WRF-Flexpart simulations during the
23 MILAGRO Field Campaign, *Atmos. Chem. Phys.*, 11, 3543-3563, <https://doi.org/10.5194/acp-11-3543-2011>, 2011.
- 24 Ehrhard, J., Khatib, I., Winkler, C., Kunz, R., Moussiopoulos, N., and Ernst, G.: The microscale model MIMO: development
25 and assessment, *J. Wind. Eng. Ind. Aerodyn.*, 85, 163-176, [https://doi.org/10.1016/S0167-6105\(99\)00137-3](https://doi.org/10.1016/S0167-6105(99)00137-3), 2000.
- 26 Fast, J. D., and Easter, R. C.: A Lagrangian particle dispersion model compatible with WRF, 7th WRF Users Workshop,
27 NCAR, 19-22, 2006.
- 28 Fernando, H., Zajic, D., Sabatino, S. D., Dimitrova, R., and Dallman, A.: Flow, turbulence, and pollutant dispersion in urban
29 atmosphere, *Phys. Fluids*, 22, 051301, <https://doi.org/10.1063/1.3407662>, 2010.
- 30 Gao, Y., Shan, H., Zhang, S., Sheng, L., Li, J., Zhang, J., Ma, M., Meng, H., Luo, K., Gao, H., and Yao, X.: Characteristics
31 and sources of PM_{2.5} with focus on two severe pollution events in a coastal city of Qingdao, China, *Chemosphere*, 247,
32 125861, <https://doi.org/10.1016/j.chemosphere.2020.125861>, 2020.
- 33 Gosman, A. D.: Developments in CFD for industrial and environmental applications in wind engineering, *J. Wind. Eng. Ind.*
34 *Aerodyn.*, 81, 21-39, [https://doi.org/10.1016/S0167-6105\(99\)00007-0](https://doi.org/10.1016/S0167-6105(99)00007-0), 1999.
- 35 He, J., Mao, H., Gong, S., Yu, Y., and Zou, C.: Investigation of particulate matter regional transport in Beijing based on
36 numerical simulation, *Aerosol Air Qual. Res.*, 17, 1181-1189, <https://doi.org/10.4209/AAQR.2016.03.0110>, 2017a.
- 37 He, J., Zhang, L., Yao, Z., Che, H., Gong, S., Wang, M., Zhao, M., and Jing, B.: Source apportionment of particulate matter
38 based on numerical simulation during a severe pollution period in Tangshan, North China, *Environ. Pollut.*, 266, 115133,
39 <https://doi.org/10.1016/j.envpol.2020.115133>, 2020.
- 40 He, J. J., Yu, Y., Liu, N., Zhao, S. P., and Chen, J. B.: Impact of land surface information on WRFs performance in complex
41 terrain area, *Chin. J. Atmos. Sci.*, 38, 484-498, <https://doi.org/10.3878/j.issn.1006-9895.2013>, 2014.
- 42 He, J. J., Yu, Y., Liu, N., and Zhao, S. P.: Impacts of uncertainty in land surface information on simulated surface
43 temperature and precipitation over China, *Int J Climatol*, 37, 829-847, <https://doi.org/10.1002/joc.5041>, 2017b.
- 44 Hendricks, E. A., Diehl, S. R., Burrows, D. A., and Keith, R.: Evaluation of a Fast-Running Urban Dispersion Modeling
45 System Using Joint Urban 2003 Field Data, *J Appl Meteorol Climatol*, 46, 2165-2179,
46 <https://doi.org/10.1175/2006JAMC1289.1>, 2007.
- 47 Heo, J., Foy, B. D., Olson, M. R., Pakbin, P., Sioutas, C., and Schauer, J.: Impact of regional transport on the anthropogenic
48 and biogenic secondary organic aerosols in the Los Angeles Basin, *Atmos. Environ.*, 103, 171-179,
49 <https://doi.org/10.1016/J.ATMOSENV.2014.12.041>, 2015.
- 50 Hopke, P., Zhou, L., and Poirot, R.: Reconciling trajectory ensemble receptor model results with emissions, *Environ. Sci.*
51 *Technol.*, 39(20), 7980-7983, <https://doi.org/10.1021/es049816g>, 2005.
- 52 Iacono, M. J., Delamere, J. S., Mlawer, E. J., Shephard, M. W., and Collins, W. D.: Radiative Forcing by Long-Lived
53 Greenhouse Gases: Calculations with the AER Radiative Transfer Models, *J. Geophys. Res.-Atmos.*, 113, D13103,
54 <https://doi.org/10.1029/2008JD009944>, 2008.
- 55 Jls, A., Bse, A., Cq, B., Ddlp, B., Am, A., Fm, A., Rb, B., Er, A., Gm, A., and Ed, A.: Performance evaluation of a multiscale
56 modelling system applied to particulate matter dispersion in a real traffic hot spot in Madrid (Spain) - ScienceDirect,
57 *Atmospheric Pollut*, 11, 141-155, <https://doi.org/10.1016/j.apr.2019.10.001>, 2020.
- 58 Kurppa, M., Hellsten, A., Auvinen, M., Raasch, S., Vesala, T., and Järvi, L.: Ventilation and Air Quality in City Blocks Using
59 Large-Eddy SimulatioŽ Urban Planning Perspective, *Atmosphere*, 9, 65, <https://doi.org/10.3390/ATMOS9020065>, 2018.
- 60 Kwak, K.-H., Baik, J.-J., Ryu, Y.-H., and Lee, S.-H.: Urban air quality simulation in a high-rise building area using a CFD
61 model coupled with mesoscale meteorological and chemistry-transport models, *Atmos. Environ.*, 100, 167-177,
62 <https://doi.org/10.1016/j.atmosenv.2014.10.059>, 2015.

1 Lei, L., Fei, H., Cheng, X. L., and Han, H. Y.: The application of computational fluid dynamics to pedestrian level wind safety
2 problem induced by high-rise buildings, *Chin. Phys. B*, 13, 1070-1075, <https://doi.org/10.1088/1009-1963/13/7/018>, 2004.

3 Lei, L. I., Yang, L., Zhang, L. J., and Jiang, Y.: Numerical Study on the Impact of Ground Heating and Ambient Wind Speed
4 on Flow Fields in Street Canyons, *Adv Atmos Sci*, 29, 1227-1237, <https://doi.org/10.1007/s00376-012-1066-3>, 2012.

5 Li, L., Hu, F., Cheng, X. L., Jiang, J. H., and Ma, X. G.: Numerical simulation of the flow within and over an intersection
6 model with Reynolds-averaged Navier-Stokes method, *Chin. Phys. B*, 15, 149-155, <https://doi.org/10.1088/1009-1963/15/1/024>, 2006.

7
8 Li, S., Sun, X., Zhang, S., Zhao, S., and Zhang, R.: A Study on Microscale Wind Simulations with a Coupled WRF-CFD
9 Model in the Chongli Mountain Region of Hebei Province, China, *Atmosphere*, 10, 731,
10 <https://doi.org/10.3390/atmos10120731>, 2019.

11 Li, X.-X., Liu, C.-H., and Leung, D. Y. C.: Large-Eddy Simulation of Flow and Pollutant Dispersion in High-Aspect-Ratio
12 Urban Street Canyons with Wall Model, *Bound. Layer Meteorol.*, 129, 249-268, <https://doi.org/10.1007/s10546-008-9313-y>,
13 2008.

14 Lin, Y. L., Farley, R. D., and Orville, H. D.: Bulk Parameterization of the Snow Field in a Cloud Model, *J APPL METEOROL*,
15 22, 1065-1092, [https://doi.org/10.1175/1520-0450\(1983\)022<1065:BPOTSF>2.0.CO;2](https://doi.org/10.1175/1520-0450(1983)022<1065:BPOTSF>2.0.CO;2), 1983.

16 Liu, N., Yu, Y., He, J., and Zhao, S.: Integrated modeling of urban-scale pollutant transport: application in a semi-arid urban
17 valley, Northwestern China (SCI), *Atmospheric Pollut. Res.*, 4, 306-314, <https://doi.org/10.5094/APR.2013.034>, 2013.

18 Liu, S., Pan, W., Zhao, X., Zhang, H., Cheng, X., Long, Z., and Chen, Q.: Influence of surrounding buildings on wind flow
19 around a building predicted by CFD simulations, *Build Environ*, 140, 1-10, <https://doi.org/10.1016/j.buildenv.2018.05.011>,
20 2018.

21 Macdonald, R. W., Griffiths, R. F., and Cheah, S. C.: Field experiments of dispersion through regular arrays of cubic structures,
22 *Atmos. Environ.*, 31, 783-795, [https://doi.org/10.1016/S1352-2310\(96\)00263-4](https://doi.org/10.1016/S1352-2310(96)00263-4), 1997.

23 Madala, S., Satyanarayana, A. N., Srinivas, C., and Kumar, M.: Mesoscale atmospheric flow-field simulations for air quality
24 modeling over complex terrain region of Ranchi in eastern India using WRF, *Atmos. Environ.*, 107, 315-328,
25 <https://doi.org/10.1016/J.ATMOSENV.2015.02.059>, 2015.

26 Mavroidis, I., Rf., G., and Dj., H.: Field and wind tunnel investigations of plume dispersion around single surface obstacles,
27 *Atmos. Environ.*, 37, 2903-2918, [https://doi.org/10.1016/S1352-2310\(03\)00300-5](https://doi.org/10.1016/S1352-2310(03)00300-5), 2003.

28 Milliez, M., and Carissimo, B.: Computational Fluid Dynamical Modelling of Concentration Fluctuations in an Idealized
29 Urban Area, *Bound. Layer Meteorol.*, 127, 241-259, <https://doi.org/10.1007/s10546-008-9266-1>, 2008.

30 Nakanishi, M., and Niino, H.: An Improved Mellor-Yamada Level-3 Model: Its Numerical Stability and Application to a
31 Regional Prediction of Advection Fog, *Bound. Layer Meteorol.*, 119, 397-407, <https://doi.org/10.1007/S10546-005-9030-8>,
32 2006.

33 Nelson, M. A., Brown, M. J., Halverson, S. A., Bieringer, P. E., Annunzio, A., Bieberbach, G., and Meech, S.: A Case Study
34 of the Weather Research and Forecasting Model Applied to the Joint Urban 2003 Tracer Field Experiment. Part 2: Gas Tracer
35 Dispersion, *Bound. Layer Meteorol.*, 161, 461-490, <https://doi.org/10.1007/s10546-016-0188-z>, 2016.

36 Park, S. B., Baik, J. J., and Han, B. S.: Large-eddy simulation of turbulent flow in a densely built-up urban area, *Environ. Fluid
37 Mech.*, 15, 235-250, <https://doi.org/10.1007/s10652-013-9306-3>, 2015.

38 Poirot, R., Wishinski, P., Hopke, P., and Polissar, A.: Comparative application of multiple receptor methods to identify aerosol
39 sources in northern Vermont, *Environ. Sci. Technol.*, 35(23), 4622-4636, <https://doi.org/10.1021/es011442t>, 2001.

40 Sada, K., and Sato, A.: Numerical calculation of flow and stack-gas concentration fluctuation around a cubical building, *Atmos.
41 Environ.*, 36, 5527-5534, [https://doi.org/10.1016/S1352-2310\(02\)00668-4](https://doi.org/10.1016/S1352-2310(02)00668-4), 2002.

42 Salvador, P., Artífano, B., Querol, X., and Alastuey, A.: A combined analysis of backward trajectories and aerosol chemistry
43 to characterise long-range transport episodes of particulate matter: the madrid air basin, a case study, *Sci. Total Environ.*,
44 390(2-3), 495-506, <https://doi.org/10.1016/j.scitotenv.2007.10.052>, 2008.

45 Sandeepan, B., Rakesh, P. T., and Venkatesan, R.: Numerical simulation of observed submesoscale plume meandering under
46 nocturnal drainage flow, *Atmos. Environ.*, 69, 29-36, <https://doi.org/10.1016/J.ATMOSENV.2012.12.007>, 2013.

47 Santiago, J. L., Rafael Borge, Fernando Martín, David de la Paz, Alberto Martilli, Lumbreras, J., and Sánchez, a. B.: Evaluation
48 of a CFD-based approach to estimate pollutant distribution within a real urban canopy by means of passive samplers., *Sci.
49 Total Environ.*, 576, 46-58, <https://doi.org/10.1016/j.scitotenv.2016.09.234>, 2017.

50 Schlünzen, K. H., and Sokhi, R. S.: Overview of Tools and Methods for Meteorological and Air Pollution Mesoscale Model
51 Evaluation and User Training, Joint report by WMO and COST 728, WMO/TD-No. 1457, Geneva, Switzerland, 2008, 2008.

52 Seidel, D. J., Zhang, Y., Beljaars, A., Golaz, J. C., Jacobson, A. R., and Medeiros, B.: Climatology of the planetary boundary
53 layer over the continental United States and Europe, *Journal of Geophysical Research Atmospheres*, 117,
54 <https://doi.org/10.1029/2012JD018143>, 2012.

55 Stam, J.: Stable Fluids, *ACM Trans. Graph.*, 1999, <https://doi.org/10.1145/311535.311548>, 1999.

56 Steenburgh, W., J., Stoll, R., Gowardhan, A., Kochanski, A., K., Brown, and M., J.: One-Way Coupling of the WRF-QUIC
57 Urban Dispersion Modeling System, *Journal of Applied Meteorology and Climatology*, *J Appl Meteorol Climatol*,
58 <https://doi.org/10.1175/JAMC-D-15-0020.1>, 2015.

59 Stohl, A.: A backward modeling study of intercontinental pollution transport using aircraft measurements, *J. Geophys. Res.*,
60 108, 4370, <https://doi.org/10.1029/2002jd002862>, 2003.

61 Stohl, A., and James, P.: A Lagrangian Analysis of the Atmospheric Branch of the Global Water Cycle. Part I: Method
62 Description, Validation, and Demonstration for the August 2002 Flooding in Central Europe, *J Hydrometeorol*, 5, 656,
63 [https://doi.org/10.1175/1525-7541\(2004\)0052.0.CO;2](https://doi.org/10.1175/1525-7541(2004)0052.0.CO;2), 2004.

1 Stohl, A., Forster, C., Frank, A., Seibert, P., and Wotawa, G.: Technical note: The Lagrangian particle dispersion model
2 FLEXPART version 6.2, *Atmos. Chem. Phys.*, 5, 2461-2474, <https://doi.org/10.5194/ACP-5-2461-2005>, 2005.

3 Stull, R. B.: *An Introduction to Boundary Layer Meteorology*, Springer Netherlands, Dordrecht,, 1988.

4 Sui, L., Jiang, M., Li, Z., and Zhou, S.: Diffusion effect analysis of pollution gas under the impact of urban three-dimensional
5 pattern, in: 5th International Conference on Energy and Environmental Protection, Shengzhen, China, 17-18, September 2016,
6 903-909, 2016.

7 Temimi, M., Fonseca, R., Reddy, N. N., Weston, M., and Naqbi, H. A.: Assessing The Impact of Changes in Land Surface
8 Conditions on WRF Predictions in Arid Regions, *J Hydrometeorol*, 21, 2829-2853, <https://doi.org/10.1175/JHM-D-20-0083.1>,
9 2020.

10 Tewari, M., Kusaka, H., Chen, F., Coirier, W. J., Kim, S., Wyszogrodzki, A. A., and Warner, T. T.: Impact of coupling a
11 microscale computational fluid dynamics model with a mesoscale model on urban scale contaminant transport and dispersion,
12 *Atmos. Res.*, 96, 656-664, <https://doi.org/10.1016/j.atmosres.2010.01.006>, 2010.

13 Voegeleang, D., and Holtslag, A.: Evaluation and model impacts of alternative boundary-layer height formulations, *Bound.-*
14 *Layer. Meteorol.*, 81, 245-269, <https://doi.org/10.1007/BF02430331>, 1996.

15 Yu, C., Zhao, T., Bai, Y., Zhang, L., Kong, S., Yu, X., He, J., Cui, C., Yang, J., You, Y., Ma, G., Wu, M., and Chang, J.:
16 Heavy air pollution with a unique “non-stagnant” atmospheric boundary layer in the Yangtze River middle basin aggravated
17 by regional transport of PM_{2.5} over China, *Atmos. Chem. Phys.*, 20, 7217-7230, <https://doi.org/10.5194/acp-20-7217-2020>,
18 2020.

19 Yu, T. Y.: Source identification of emission sources for hydrocarbon with backward trajectory model and statistical methods,
20 *Pol. J. Environ. Stud.*, 26(2), 893-902, <https://doi.org/10.15244/pjoes/65744>, 2017.

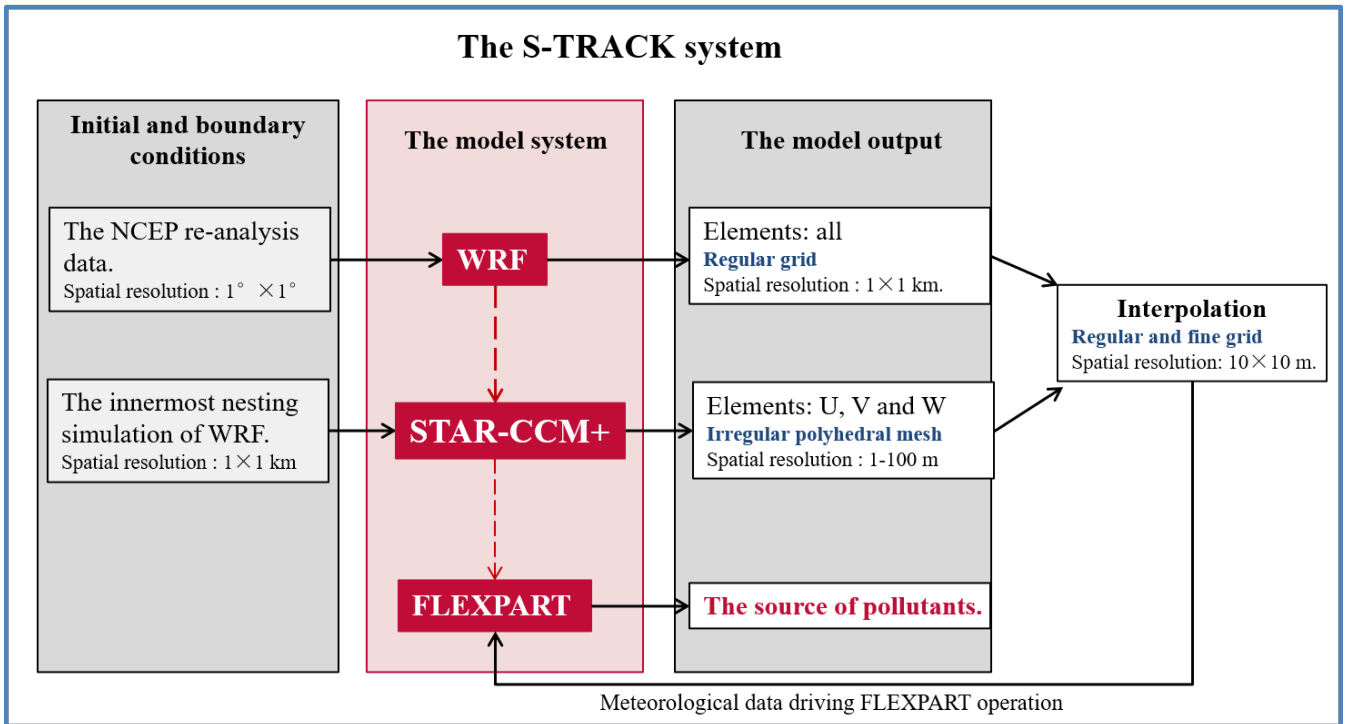
21 Yucong, Miao, Shuhua, Liu, Hui, Zheng, Yijia, Zheng, Bicheng, and Chen: A multi-scale urban atmospheric dispersion model
22 for emergency management, *Adv Atmos Sci*, 31, 13, <https://doi.org/10.1007/s00376-014-3254-9>, 2014.

23 Zhang, H., Xu, T., Zong, Y., Tang, H., Liu, X., and Wang, Y.: Influence of Meteorological Conditions on Pollutant Dispersion
24 in Street Canyon, *Procedia Engineering*, 121, 899-905, <https://doi.org/10.1016/J.PROENG.2015.09.047>, 2015.

25 Zhang, H., Tang, S., Yue, H., Wu, K., Zhu, Y., Liu, C.-J., Liang, B., and Li, C.: Comparison of Computational Fluid Dynamic
26 Simulation of a Stirred Tank with Polyhedral and Tetrahedral Meshes, *Iran. J. Chem. Chem. Eng.*, 39, 311-319,
27 <https://doi.org/10.30492/IJCCE.2019.34950>, 2020.

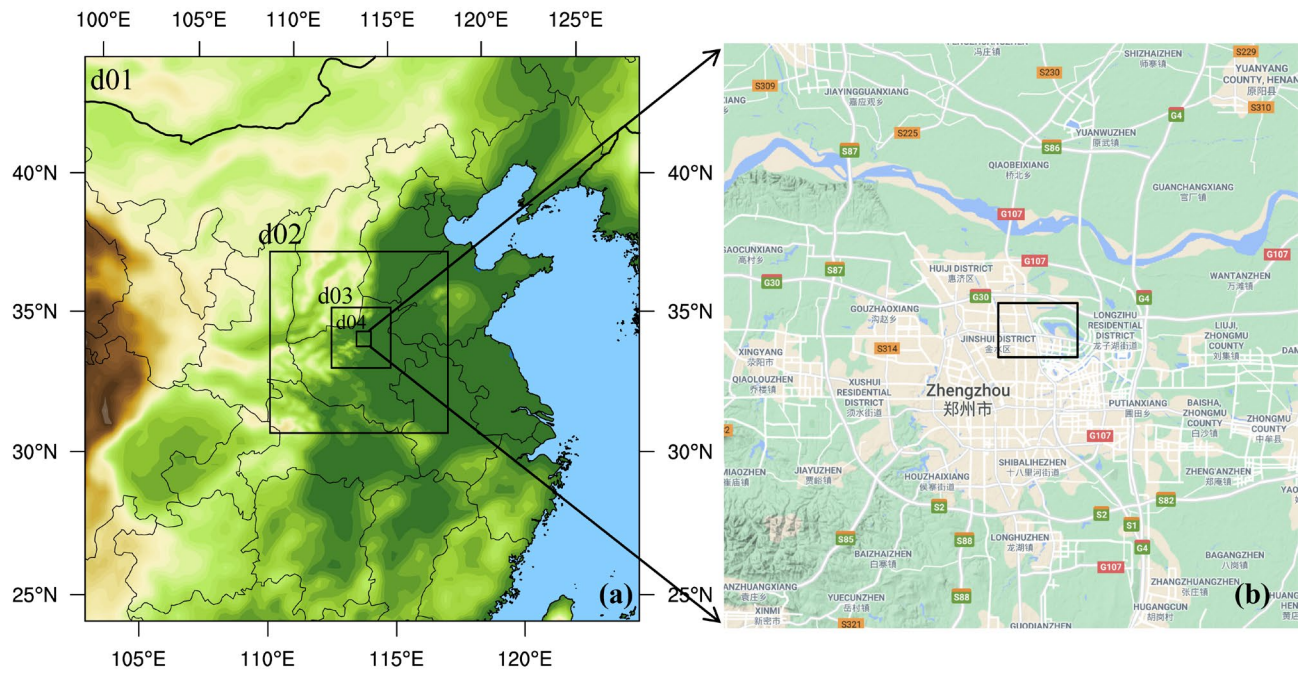
28 Zheng, Y., Miao, Y., Liu, S., Chen, B., Zheng, H., and Wang, S.: Simulating Flow and Dispersion by Using WRF-CFD
29 Coupled Model in a Built-Up Area of Shenyang, China, *Adv. Meteorol*, 2015, 1-15, <https://doi.org/10.1155/2015/528618>,
30 2015.

31



1
 2 **Figure 1: The S-TRACK system: The role of WRF, STAR-CCM+ and FLEXPART in the S-**
 3 **TRACK system and the process of gradual refinement of resolution.**

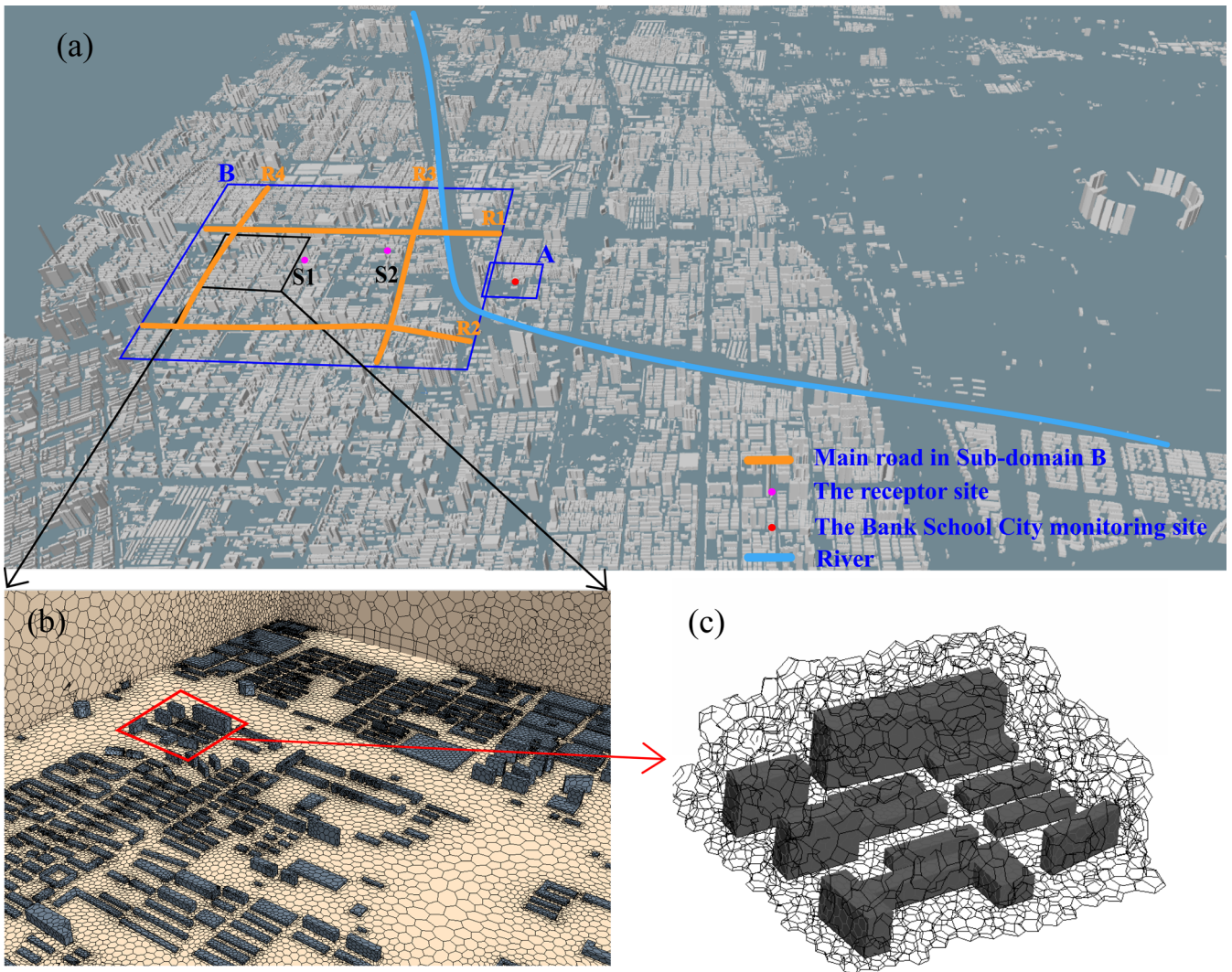
4



1

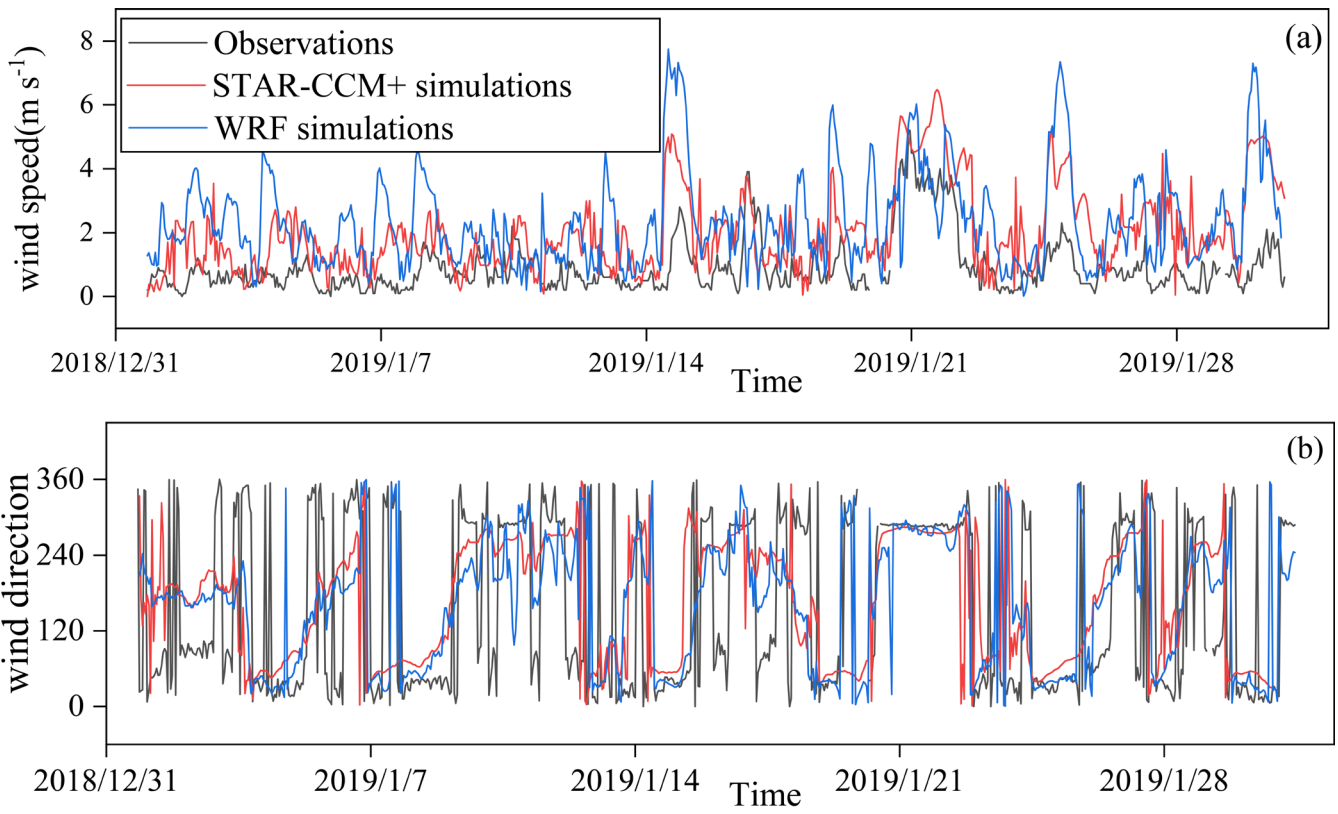
2 **Figure 2: Domain configuration of the WRF model: (a) the range of the four nested domains (d1-**
 3 **d4); (b) the innermost nested domain (d4), within which the black box represents the STAR-CCM+**
 4 **simulation domain (extracted from © Google Maps 2021).**

5



1
 2 **Figure 3: The computational domain of the STAR-CCM+ is shown in (a). The sub-domain A is used**
 3 **for detailed analysis of the wind environment, and the Bank School City (BSC) monitoring site is**
 4 **marked with the red dot. Sub-domain B is used to analyse the potential contribution of traffic**
 5 **source on receptor sites in the region, with magenta dots (S1 and S2) indicating the receptor sites**
 6 **and Orange line indicating the main roads. The polyhedral mesh is used to divide the STAR-CCM+**
 7 **simulation area. The mesh details of the vertical cross section and building surface are shown in**
 8 **(b), and the 3D meshes are shown in (c).**

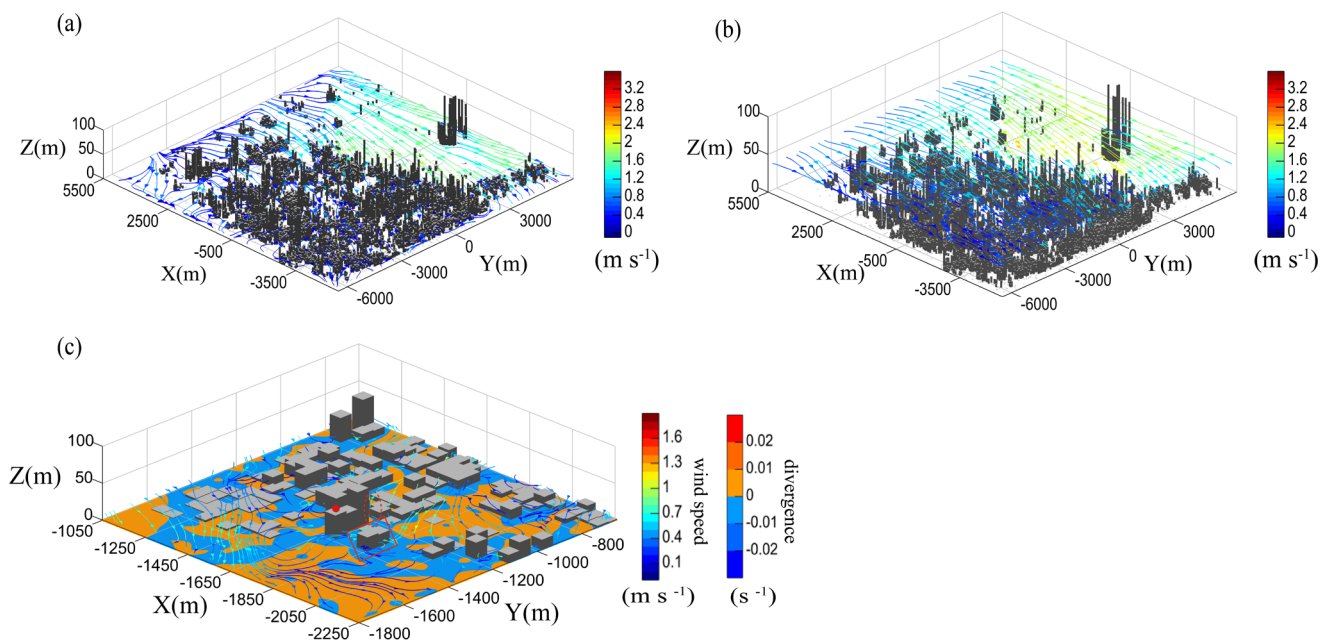
9



1

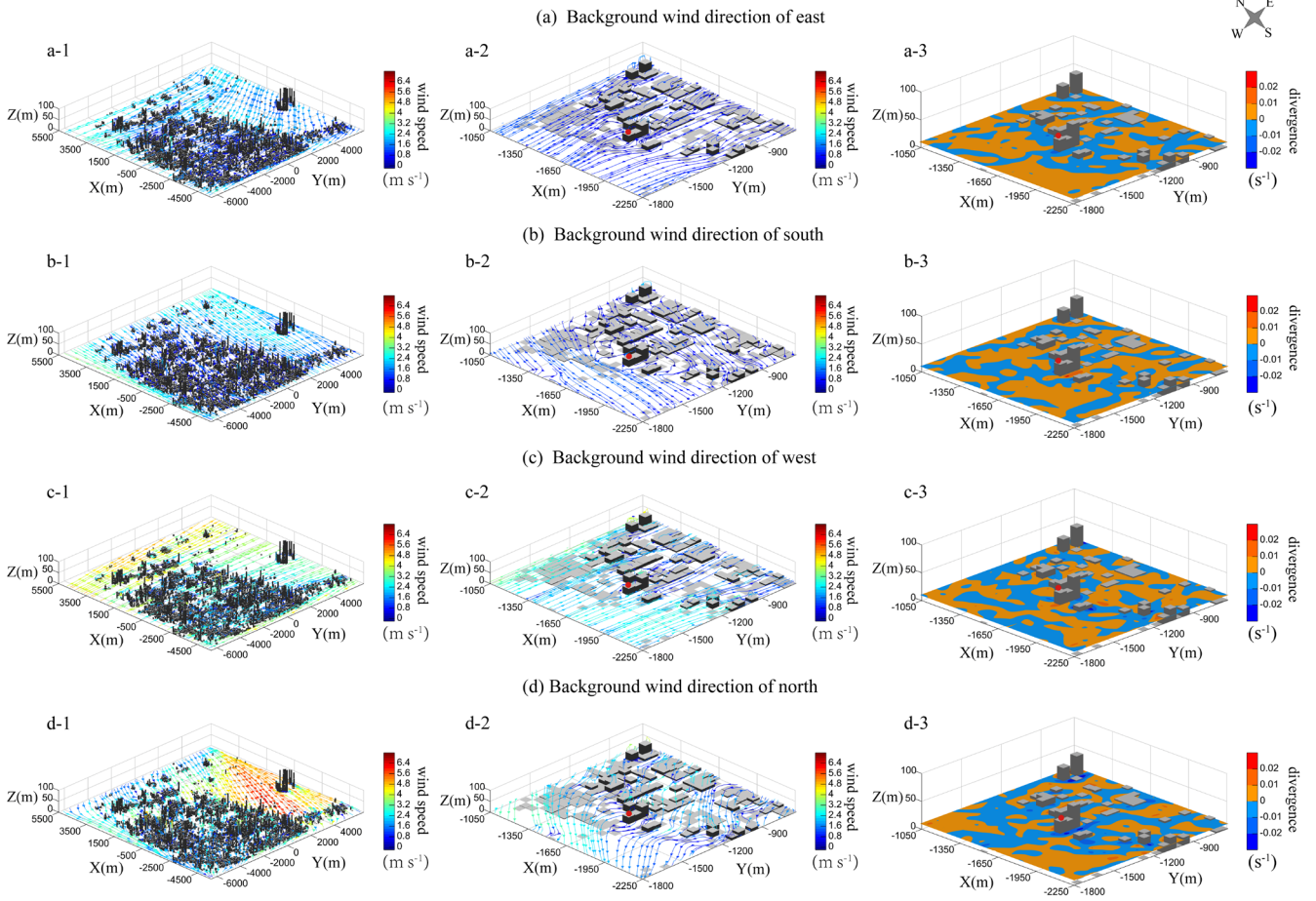
2 **Figure 4: Evaluation of the wind simulation results at the BSC monitoring site (see in Fig. 3a): the**
 3 **simulated, by WRF (blue line) and STAR-CCM+ (red line) model, respectively, and the observed**
 4 **(grey line) hourly near-surface wind speeds (a) and wind directions (b).**

5



1
 2 **Figure 5: The simulated wind streamlines at the height of 5 m (a) and 40 m (b) averaged in January**
 3 **2019 in the whole S-TRACK simulation domain; the simulated wind streamlines and divergence (c)**
 4 **at the near-surface averaged in January 2019 in the sub-domain A (see in Fig. 3a). The BSC**
 5 **monitoring site is marked with red dot.**

6



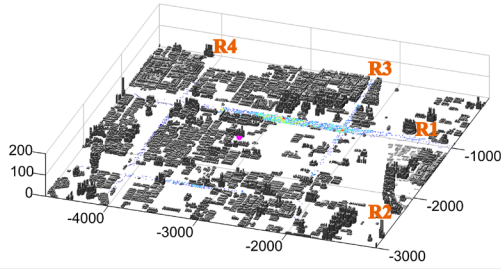
1

2 **Figure 6: The wind field streamlines and divergences under the background wind directions of east**
3 **(a), south (b), west (c) and north (d). The BSC monitoring site is marked with red dot.**

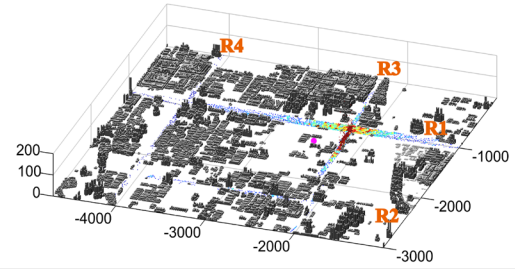
4

1

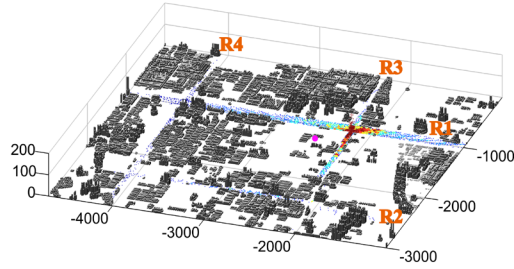
(a) Receptor site S1 (h = 2 m)



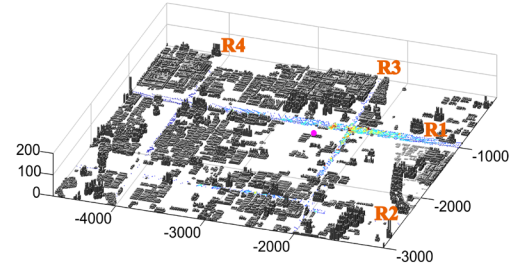
(b) Receptor site S2 (h = 2 m)



(c) Receptor site S5 (h = 15 m)



(d) Receptor site S7 (h = 40 m)

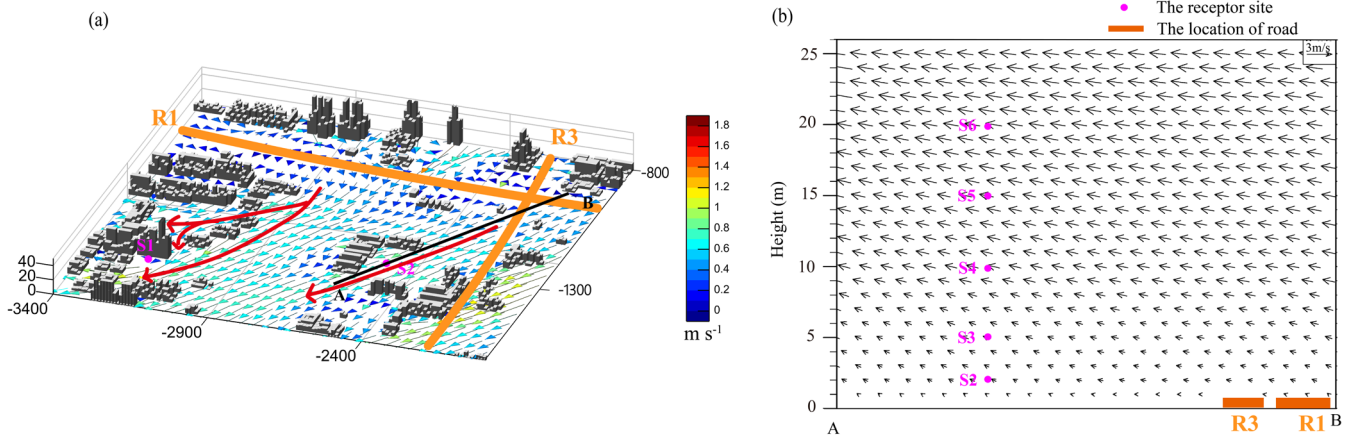


2

3 **Figure 7: Density distribution of all trajectory points passing through the traffic roads that received**
4 **from different receptor sites (S1, S2, S5, and S7, see details in Table 4). The four receptor sites are**
5 **all marked with magenta dots.**

6

1



2

3 **Figure 8: The (a) average surface wind and (b) vertical structure of average winds that along the**
4 **wind direction around the receptor site S2 (line AB) in January 2019. The road R1 is marked with**
5 **orange line; the location of the vertical profile is shown in black line, and the receptor sites S1 to S6**
6 **are all marked with magenta dots.**

7

8

1 **Table 1. The list of variables required to run FLEXPART and the sources of variables.**

variable	Description	Source
PB	base value of pressure	WRF
P	perturbation of pressure	WRF
PHB	base value of geopotential	WRF
PH	perturbation of geopotential	WRF
T	temperature	WRF
QVAPOR	specific humidity	WRF
MAPFAC_M	map factor	WRF
PSFC	surface pressure	STAR-CCM+
U10	10 m wind along x axis	STAR-CCM+
V10	10 m wind along y axis	STAR-CCM+
T2	2 m temperature	WRF
Q2	2 m dew point	WRF
SWDOWN	surface solar radiation (optional)	WRF
RAINNC	large scale precipitation (optional)	WRF
RAINC	convective precipitation (optional)	WRF
HFX	surface sensible heat flux (optional)	STAR-CCM+
U	wind along x axis	STAR-CCM+
V	wind along y axis	STAR-CCM+
W	Cartesian vertical velocity	STAR-CCM+

2

3 **Table 2 Parameterization scheme for the physical processes set up in the WRF model.**

Physical management	Parameterization	Reference
Microphysics scheme	Lin	Lin et al. (1983)
Longwave radiation scheme	RRTMG	Iacono et al. (2008)
Shortwave radiation scheme	RRTMG	Iacono et al. (2008)
Land surface scheme	Noah	Chen and Dudhia (2001)
Planetary boundary layer scheme	MYNN3	Nakanishi and Niino (2006)

4

5

6

7 **Table 3 Statistical performances of the hourly near-surface meteorology simulated by the WRF model.**

	R	MB	ME	RMSE
T	0.80	-1.86 (K)	2.33 (K)	2.82 (K)
RH	0.70	-5.95 (%)	11.5 (%)	15.0 (%)
P	0.98	3.66 (hPa)	3.66 (hPa)	3.77 (hPa)
WS	0.45	1.44 (m s^{-1})	1.58 (m s^{-1})	1.97 (m s^{-1})

8

9 **Table 4. Locations of receptor sites and the corresponding PCR.**

Receptor site	Location (x, y, z)	PCR				
		R1	R2	R3	R4	All
S1	(-3200 m, -1420 m, 2 m)	1.81%	-	-	-	-
S2	(-2500 m, -1300 m, 2 m)	2.38%	0.18%	1.32%	0.16%	4.05%
S3	(-2500 m, -1300 m, 5 m)	2.57%	0.29%	1.28%	0.10%	4.25%
S4	(-2500 m, -1300 m, 10 m)	2.71%	0.32%	1.18%	0.12%	4.33%
S5	(-2500 m, -1300 m, 15 m)	2.98%	0.27%	1.22%	0.20%	4.67%
S6	(-2500 m, -1300 m, 20 m)	2.75%	0.37%	1.09%	0.17%	4.38%
S7	(-2500 m, -1300 m, 40 m)	2.30%	0.39%	0.70%	0.25%	3.64%
S8	(-2500 m, -1300 m, 50 m)	1.94%	0.57%	0.68%	0.36%	3.55%

1

2